System-Reliability-based Disaster Resilience Analysis for Structures Considering Aleatory Uncertainties in External Loads

Sang-ri Yi[1], **and Taeyong Kim**[2*]

[1] Department of Civil and Environmental Engineering, University of California Berkeley, Berkeley, USA
[2] Department of Civil Systems Engineering, Ajou University, Suwon, Republic of Korea
* Correspondence: taeyongkim@ajou.ac.kr; Tel.: +82-31-219-2505

Submitted: April 12, 2023; Revised Manuscript Submitted: July 3, 2023

Abstract: The concept of disaster resilience is getting more prominent in the era of climate change due to the increase in the intensities and uncertainties of disaster events. To effectively assess the holistic capacity of structural systems, a disaster resilience analysis framework has been recently developed from a system-reliability-based perspective. The framework evaluates resilience in terms of reliability, redundancy, and recoverability and provides quantitative indices of reliability and redundancy for structures with a resilience threshold. Although this framework enables the comprehensive evaluation of disaster resilience performance, practical applications of such concepts to the structures subjected to dynamic excitations with large aleatory uncertainty, such as earthquakes, remain challenging. This study develops a framework to assess the resilience performance of structures by taking into account the aleatory uncertainties in external forces. Along with the development of reliability and redundancy curves that can effectively accommodate such excitations, a new resilience threshold representation is proposed to incorporate recoverability in the decision-making process. Moreover, we provide efficient procedures for calculating the reliability and redundancy curves to alleviate the computational complexity during the resilience analysis. Two earthquake application examples are presented targeting a nine-story building and a cable-stayed bridge system to demonstrate the enhanced practical applicability of the proposed framework.

Keywords: Earthquake excitations; Structural system reliability; Resilience criteria; Resilience-based engineering; Aleatoric uncertainty

1. Introduction

Civil infrastructures are designed to limit the extent of damages for frequent hazardous events, and further, to ensure life safety under extreme hazardous events. The growing complexity of urban communities complicates the prediction of disaster performance and challenges the associated design decisions. Furthermore, the effects of such mispredictions are often extended to the recovery stages, demanding significant time and resources to regain the pre-event condition. As a result, there is a growing emphasis on incorporating long-term outcomes in the disaster risk management framework, such as technical, environmental, economic, and social consequences. To account for the broader impact of disasters, the risk management paradigm is being shifted from “fail-safe” to “safe-to-fail” (Ahern, 2011) – motivating the introduction of resilient infrastructure.

While disciplines such as physics, psychology, and economics, have been using different definitions for resilience, in the context of structural engineering, resilience is defined as the holistic ability or capacity of a structure to “sustain internal and external disruptions without discontinuity of the original functionality or, if discontinued, to recover fully and rapidly (ASME, 2009).” Based on the concept, a series of studies were undertaken to develop the criteria and methodologies for evaluating the resilience performance of civil structural systems (Bruneau et al., 2003; Lim et al., 2022). A framework consisting of four attributes - robustness, redundancy, resourcefulness, and rapidity -

is the most widely used resilience concept in the structural engineering field (Bruneau et al., 2003). Furthermore, by adopting the 'resilience triangle model,' i.e., a variant of that shown in Figure 1(a), to represent the initial loss after a disaster and the following restoration of the system functionality, many researchers have proposed different indices, metrics, and frameworks to assess the resilience performance of structural systems (Didier et al., 2018; Hosseini et al., 2016; Jiang et al., 2020; Rathnayaka et al., 2022). Although the framework enables quantitative assessment of the initial loss and the recovery process considering various uncertainties, Lim et al. (2022) identified its three critical limitations. First, the restoration curve models are often arbitrarily chosen by the modelers, which may lead to different resilience performance evaluations. Second, although the underlying structural functionality is determined by an intertwined relationship between components- and system-level performances, most of the research efforts based on the resilience triangle focused on estimating the resilience performance of either structural components or systems only. Third, it may not be straightforward to employ the resilience triangle framework in post-disaster decision-making because the component/system performances are often aggregated into a single measure, such as the area of the triangle.

To address such issues, Lim et al. (2022) proposed a new concept of disaster resilience from a system-reliability perspective. In their work, disaster resilience is characterized by three criteria, i.e., reliability, redundancy, and recoverability, and the roles of the criteria are delineated at the individual structure level. In the analysis, the resilience performance is described by inspecting possible sequences of the progressive system failure scenarios. For each *initial disruption scenario*, reliability (β), redundancy (π), and recoverability indices are computed and presented in a single plot as shown in Figure 1(b). Note that the recoverability index is visualized by a color. Such a two-dimensional scattered plot is termed the β-π diagram in Lim et al. (2022), and is used to visualize the resilience performance of the structure. Moreover, those reliability and redundancy indices are capable of not only describing the likelihood of each disruption scenario but also identifying the fatal disruption cases by introducing a resilience performance limit – in terms of per-hazard *de minimis* level of risk. The *de minimis* risk stands for a threshold value of the annual system failure probability given a hazard below which a society normally does not impose any regulations (Paté-Cornell, 1994). This allows the β-π diagram to provide an instantaneous intuition on the likelihood of each disruption scenario (as a coordinate of β) and its impact (as a coordinate of π), as well as to define the system-level safety limit, i.e., resilience limit, in terms of the two indices.

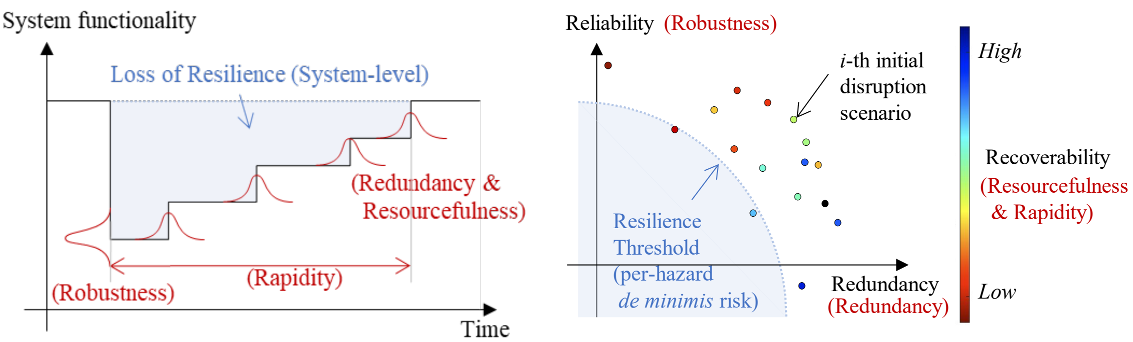

(a) Resilience triangle model (b) System-reliability-based resilience assessment

Figure 1. Illustrative comparison of resilience triangle (left) with four resilience attributes (red), and system-reliability-based resilience diagram (right) with three resilience criteria (black)

Although Lim et al. (2022) effectively addressed the limitations of the resilience triangle model, the practical application of the concept to structures under realistic loading conditions, e.g., earthquakes, remains challenging because of the following three reasons. First, since Lim et al. (2022) proposed the resilience indices focusing on the structural systems subjected to static loads, it is not straightforward to calculate such indices under the presence of high stochastic aleatory uncertainties. In other words, new formulations need to be derived for the reliability and redundancy indices that consider the aleatoric uncertainty characteristics of external loads (i.e., the inherent randomness that cannot be explained by feature variables) and their impacts on the systems. Second, the initial disruption scenarios are defined as mutually exclusive and collectively exhaustive (MECE) events, but a procedure to obtain the resilience metrics for each MECE event was hardly addressed in Lim et al. (2022) limiting the widespread adoption of the method in real-world applications. Third, it is computationally demanding to evaluate a set of β and π when a large number of structural components are considered; yet no efficient methods have been proposed.

To address these research needs within the system-reliability-based resilience assessment framework, we aim to develop new formulations and algorithms that can accommodate earthquakes or earthquake-like dynamic excitations, which we refer to as "stochastic" excitations in this context. Note that the term "stochasticity" pertains to the "aleatoric characteristic" of the hazards and is not related to certain excitation (ground motion) models. In other words, the application of the proposed method is not limited to stochastic ground motion models, as demonstrated in the examples.

After a literature review of the system-reliability-based disaster resilience framework, we newly formulate reliability and redundancy indices for structures exposed to stochastic excitations in Section 2. Motivated by the traditional performance-based engineering formulations which utilize fragility curves and total probability theorem, the new indices are built upon the concepts of reliability and redundancy curves. Furthermore, an improved resilience performance limit is proposed from the concept of factored *de minimis* risk. In addition to the definitions, the essential pieces of information required in resilience assessment are listed to show the framework at a glance and promote its practical applications. With an example of a three-story building structure exposed to earthquake excitations, the relationship between component failure and initial disruption scenarios represented by MECE events is thoroughly investigated. Section 3 proposes several efficient methods to reduce the computational demands in estimating the reliability and redundancy curves. To demonstrate the applicability and merits of the proposed method, the framework is applied to two earthquake engineering examples in Section 4. The paper concludes with a summary and discussion in Section 5.

2. System-Reliability-based Resilience Assessment of Structures under Dynamic Excitations with High Aleatory Uncertainty

The resilience performance of structural systems should be defined by joint states of statistically dependent components and their interrelationship (Song et al., 2021). To consider such characteristics in the resilience performance assessment, Lim et al. (2022) characterized disaster resilience using three criteria, i.e., reliability, redundancy, and recoverability, and developed reliability (β) and redundancy (π) indices for individual structures. The indices have limitations to a direct application to structures under earthquake ground motions or wind forces, which is characterized by high aleatory uncertainties. Thus, in this section, after reviewing the resilience indices in Lim et al. (2022), a new disaster resilience assessment framework is proposed to embrace the aleatoric characteristics of external forces. It is remarked that since the recoverability should be evaluated considering various factors of socioeconomic impacts, this study focuses on proposing reliability and redundancy indices and their relationship, while the recoverability index will be discussed more conceptually.

2.1. Review of system-reliability-based resilience indices

In Lim et al. (2022), the resilience criteria – reliability, redundancy, and recoverability – of a structure are proposed to be evaluated considering multiple progressive failure scenarios. In particular, given a system failure path or an "initial disruption scenario," the initial component failures triggered by the external loads represent the lack of "reliability" of the system, and the subsequent system failure induced by both the external loads and the initial component disruptions are represented by the lack of "redundancy." In other words, the reliability index represents the capability of structural elements, such as columns, joints, or cables, to avoid significant initial disruptions while the redundancy index requires to reflect the system's capability in preventing a system-level failure after some structural members' disruption. The third resilience criterion, recoverability, on the other hand, is associated with the repair time and costs of structural elements to recover the original (or desired) level of safety or functionality of the structure. Thus, the three criteria are evaluated for different "initial disruption scenarios" (and different hazard types), and the collection of those values determines the overall system-level resilience.

Let us consider i-th initial disruption scenario F_i and j-th hazard event H_j. The initial disruption scenarios are defined as different possible combinations of structural component failure events that occur immediately after an extreme hazard event, and the hazard is an event that induces external forces on structural systems. The reliability index for F_i is formulated in terms of the probability of F_i given H_j, i.e.,

$$\beta_{i,j} = -\Phi^{-1}\left(P\left(F_i \middle| H_j\right)\right) \tag{1}$$

where $\Phi^{-1}(\cdot)$ denotes the inverse cumulative distribution function (CDF) of the standard Gaussian distribution. On the other hand, the redundancy index is defined in terms of the probability of system-level failure given F_i and H_j, i.e.,

$$\pi_{i,j} = -\Phi^{-1}\left(P\left(F_{sys} \middle| F_i, H_j\right)\right) \tag{2}$$

where F_{sys} denotes the system-level failure of the given structure. For the recoverability index, Lim et al. (2022) employed the economic losses of the system for the given component disruption scenario. The reliability, redundancy, and recoverability indices estimated for each disruption scenario (i) and hazard type (j) are then used to plot β–π diagram (see Figure 1(b)), which is a two-dimensional scatter plot between $\beta_{i,j}$ and $\pi_{i,j}$ with the colors representing the recoverability.

Given that the initial disruption scenarios are mutually exclusive and collectively exhaustive (MECE), the unconditional annual failure probability of structural systems associated with the hazard H_j, $P(F_{sys,j})$, can be expressed by the two resilience indices as follows:

$$P\left(F_{sys,j}\right) = \sum_i P\left(F_{sys,i,j}\right) = \sum_i P\left(F_{sys} \middle| F_i, H_j\right) P\left(F_i \middle| H_j\right) \lambda_{H_j} = \sum_i \Phi\left(-\pi_{i,j}\right)\Phi\left(-\beta_{i,j}\right)\lambda_{H_j} \tag{3}$$

where $P(F_{sys,i,j})$ stands for the annual probability of the system failure event originated from the i-th initial disruption scenario under H_j, and λ_{H_j} represents the annual mean occurrence rate of H_j. The upper threshold of $P(F_{sys,j})$ or $P(F_{sys,i,j})$ should be decided based on social consensus. To this aim, Lim et al. (2022) employed the concept of *de minimis* risk (Ellingwood, 2006), the highest tolerable risk level in society, which is in the order of $10^{-7}/yr$ for the civil structural systems (Paté-Cornell, 1994). Using the *de minimis* risk level P_{dm} as the threshold, the following resilience constraint was obtained as

$$P\left(F_{sys,i,j}\right) = \Phi\left(-\pi_{i,j}\right)\Phi\left(-\beta_{i,j}\right)\lambda_{H_j} < P_{dm} \tag{4}$$

Dividing Eq. (4) by λ_{H_j}, the inequality can be written as

$$\Phi\left(-\pi_{i,j}\right)\Phi\left(-\beta_{i,j}\right) < P_{dm}/\lambda_{H_j} \tag{5}$$

where P_{dm}/λ_{H_j} stands for the per-hazard *de minimis* risk. By intertwining with the β–π diagram, it is possible to quantitatively assess the resilience performance of the structure, and further identify the critical components associated with the risky scenarios.

Nonetheless, the original resilience threshold in Eq. (5) reveals two limitations. First, recoverability is not explicitly considered in Eq. (5), while it is important to incorporate recoverability into the resilience assessment to obtain a more comprehensive understanding of the system's ability to withstand and recover from disruptions. The second limitation pertains to the use of per-hazard *de minimis* risk as a resilience limit. While the framework allows for versatile choices of initial disruption scenario definitions, imposing the same per-hazard *de minimis* risk resilience threshold for different possible granularity of initial scenarios can potentially lead to over/under-estimation of the resilience performance. As an example on the extreme end, when the initial disruption scenarios are decomposed into a large number of sub-scenarios with extremely small occurrence probabilities, it is likely that all scenarios will satisfy the resilience threshold regardless of design details. This may not accurately reflect the resilience performance of the system, and to avoid this, the resilience threshold should be defined such that it is (approximately) inversely proportional to the total number of alternative failure paths considered in the analysis.

2.2. Disaster resilience assessment framework to consider aleatory uncertainties

Two contributions are made in this section to develop a system-reliability-based disaster resilience assessment framework of structures under stochastic excitations. First, a new concept of reliability and redundancy curves is proposed to deal with the variabilities of stochastic excitations. Second, a new resilience limit-state surface that accounts for the recoverability and the different granularity of the initial disruption scenarios is proposed.

2.2.1. Reliability and redundancy indices for stochastic excitations

The resilience indices in Eqs. (1) and (2) are applicable to general types of individual structures. However, it is challenging to apply the current formulation of such indices to the structures subjected to stochastic excitations because of the high-dimensional nature in its randomness. To consider the variabilities in stochastic excitations in the system-reliability-based resilience framework, the concept of conditional probability expression of the structural response is introduced, which is widely adopted in the traditional performance-based engineering formulation represented as the fragility analysis. Intensity measure(s) (*IM or im*) are introduced to represent the stochastic excitations, and the failure probability of components and system (reliability and redundancy analysis, respectively) are evaluated conditional to im.

Using this concept, the probability of the i-th failure scenario given a hazard event H can be written through the total probability theorem as follows:

$$P(F_i|H) = \int P(F_i|im, H) f_{IM}(im|H) dim \tag{6}$$

where $P(F_i|im, H)$ is the scenario-level fragility given the hazard event H, termed as the "reliability curve," and $f_{IM}(im|H)$ is the probability density function (PDF) of im given the hazard event H. For example, the hazard event H for an earthquake event can be characterized by various features such as source and site conditions. On the other hand, the seismic event, which represents the site-specific realizations of ground motions for a given hazard event, is featured by intensity measures that inherently involve significant amount of aleatory uncertainty. The term $P(F_i|im, H)$ captures the effect of the aleatory uncertainty of the latter. For the sake of notational simplicity, we hereafter omit the subscript j in H (i.e., H_j in Eqs. (1) and (2)) to consider only a single hazard scenario.

In a similar manner, the probability of a system-level failure given the i-th disruption scenario caused by the hazard event H is

$$P(F_{sys}|F_i, H) = \int P(F_{\text{sys}}|F_i, im, H) f_{IM}(im|F_i, H) dim \tag{7}$$

in which $P(F_{\text{sys}}|F_i, im, H)$ represents the system-level fragility induced by the i-th initial disruption scenario given the hazard event H, termed as the "redundancy curve," and $f_{IM}(im|F_i, H)$ is the PDF of im given F_i and H. Note that, not only the redundancy curve is conditioned on F_i but the distribution of im is also updated after F_i has occurred. For example, an unlikely failure of a strong component or simultaneous failure of multiple components may indicate that the applied intensity of the stochastic excitation was high, and such a strong excitation is likely to cause the subsequent system failure. $f_{IM}(im|F_i, H)$ can be obtained through Bayes' theorem as follows:

$$f_{IM}(im|F_i, H) = \frac{P(F_i|im, H) f_{IM}(im|H)}{P(F_i|H)} \tag{8}$$

By substituting Eq. (8) into Eq. (7), $P(F_{sys}|F_i, H)$ becomes

$$P(F_{sys}|F_i, H) = \frac{1}{P(F_i|H)} \int P(F_{\text{sys}}|F_i, im, H) P(F_i|im, H) f_{IM}(im|H) dim \tag{9}$$

which involves both the reliability and redundancy curves as well as $P(F_i|H)$. Following Eqs. (1) and (2), generalized reliability and redundancy indices are written as follows:

$$\beta_i = -\Phi^{-1}\big(P(F_i|H)\big) = -\Phi^{-1}\left(\int P(F_i|im, H) f_{IM}(im|H) dim\right) \tag{10}$$

$$\pi_i = -\Phi^{-1}\left(P(F_{sys}|F_i, H)\right) = -\Phi^{-1}\left(\frac{1}{P(F_i|H)} \int P(F_{\text{sys}}|F_i, im, H) P(F_i|im, H) f_{IM}(im|H) dim\right) \tag{11}$$

The dependency between the random variables of hazard and structural system in the reliability and redundancy analyses are graphically summarized in Figure 2 (a) and (b), respectively. Figure 2(b) indicates that F_i and F_{sys} are dependent on the same im. This implicitly assumes that the hazard event that causes the initial disruption (in the reliability analysis context) is the event that triggers the system failure (in the redundancy analysis context). In such a case, the observation of F_i changes the distribution of im as in Eq. (8), and the redundancy index should consider this as in Eq. (11). However, when one wants to consider a case where each of the initial disruptions and the system failure occurs due to a sequence of independent hazard realizations, e.g., a sequence of main and aftershocks, unconditional $f_{IM}(im|\, H)$ should be used instead of Eq. (8) to estimate the redundancy index as

$$\pi_i = -\Phi^{-1}\left(P\left(F_{sys}\middle|F_i, H\right)\right) = -\Phi^{-1}\left(\int P\left(F_{\text{sys}}\middle|F_i, im, H\right) f_{IM}(im|H)dim\right) \tag{12}$$

instead of Eq. (11). Under such assumptions, no arrow exists between IM and F_i in Figure 2(b), indicating the IMs in Figure 2(a) and (b) are treated as independent variables. In short, Eqs. (10) and (11) are employed for the resilience assessment of structures under a single event, while Eqs. (10) and (12) assume sequential events. The focus of this paper lies on the former.

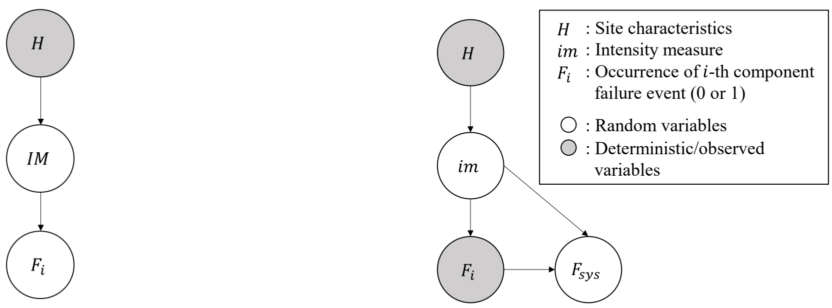

(a) Reliability analysis (b) Redundancy analysis

Figure 2. Probabilistic relationship between hazard/structural random variables

2.2.2. New resilience limit-state to account for the recoverability and granularity of the initial disruption scenarios

In the original work of Lim et al. (2022), the per-hazard *de minimis* risk P_{dm}/λ_H was employed as the resilience threshold (Eq. (5)) in the disaster resilience assessment framework. While P_{dm}/λ_H effectively incorporates the reliability and redundancy performance taking into account the annual occurrence rate of hazard, it does not explicitly consider the recoverability characteristics of each initial disruption scenario nor the number of MECE initial disruption scenarios.

To address these limitations, we propose a factored *de minimis* risk, denoted as $P^*_{dm,i}$, by multiplying the original *de minimis* risk to the recoverability index and dividing it by the number of MECE events:

$$P^*_{dm,i} = \gamma_i P_{dm}/N_F \tag{13}$$

where γ_i is a recoverability index given the i^{th} component disruption scenario F_i, which should always be positive, and N_F represents the number of MECE events. The recoverability index in Eq. (13) plays a role as a scenario-specific reduction/amplification factor and its values are determined considering various socioeconomic parameters (e.g., importance of structure, social and economic factors, availability of engineers, and community capital). Meanwhile, $P^*_{dm,i}$ decreases as the granularity of the MECE events increases. Note that $\gamma_i P_{dm}$ represents a system-level resilience threshold, i.e., maximum allowable annual failure probability of structural system, where all possible failure paths are aggregated (consider the case of $N_F = 1$ in Eq. (13)).

Using the factored *de minimis* risk, Eq. (5) can be rewritten as

$$\frac{\Phi(-\pi_i)\Phi(-\beta_i)}{\gamma_i} < P_{dm}/(\lambda_H N_F) \tag{14}$$

This enables the comprehensive assessment of the resilience performance incorporating all three criteria, and accounting for the level of granularity in the selected initial disruption scenarios. For instance, if an investigated disruption scenario does not have enough recoverability performance (i.e., low γ_i), the resilience threshold becomes more stringent (i.e., low P^*_{dm}/λ_H) requiring higher values of reliability and redundancy indices to satisfy Eq. (14). Furthermore, if the number of MECE events is extremely large, the resilience threshold again becomes more stringent. Such adjustment allows the framework to be less affected by the arbitrary selection of MECE events. The relationship between the three indices with the resilience limit *surface* is visually illustrated in Figure 3. We refer to this three-dimensional scatter plot as a "β–π–γ diagram."

Finally, it is remarked that one notable merit of the system-reliability resilience analysis framework is the clear separation of the recoverability index from the other two indices. This is attributed to the fact that each of the three resilience indices is directly conditioned on the initial disruption scenarios. This facilitates interdisciplinary communications and collaborations by allowing engineers to focus on assessing the "structural" performance only, while social scientists only aim at evaluating the recoverability performance for each initial disruption scenario without demanding onerous efforts to understand complex structural failure mechanisms. Ongoing research is being conducted to further demonstrate this concept, and the numerical examples in this study focus on the reliability and redundancy indices only, by assuming $\gamma = 1$.

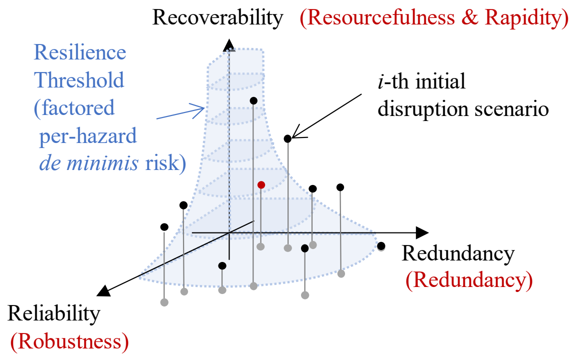

Figure 3. β–π–γ diagram and new resilience threshold

2.3. Required information in the resilience assessment framework

The assessment of resilience performance for structures subjected to stochastic excitations requires five essential pieces of information: (1) hazard model, (2) initial disruption scenarios, (3) component-level limit-state, (4) component damage model and system-level limit-state, and (5) socioeconomic information. Figure 4 depicts the roles of each feature adopting the illustrational analogy in Lim et al. (2022). The detailed descriptions associated with the five features are illustrated in the following paragraph with an example of a three-story building structure under seismic hazard environments to facilitate a comprehensive understanding.

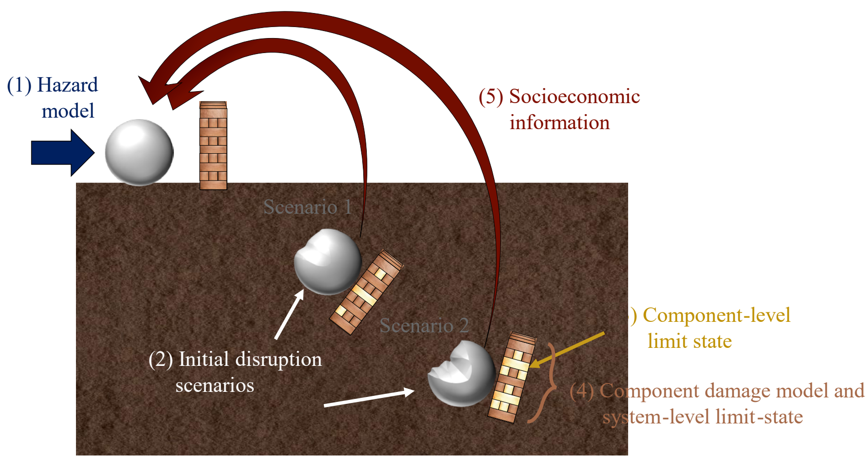

Figure 4. Five critical features for the system-reliability-based resilience assessment

- **Target Structure**

A numerical model of the target structure is required to estimate the reliability and resilience curves used in Eqs. (10) and (11), respectively. As an example, Figure 5 shows a three-story, four-bay SAC building structure which is designed by Brandow & Johnston Associates as a benchmark structure in the SAC joint venture project. The design meets the seismic code of typical low- and medium-rise buildings located in Los Angeles, California. A numerical simulation model is constructed in OpenSees (McKenna, 2011) utilizing a bilinear material (Steel 01) and a fiber section for both beams and columns. Each story consists of a weak column on the rightmost side of the building, and a rigid diaphragm assumption has been made. The first mode period of the structure is estimated as 1.01 sec, and further details of modeling parameters including material properties are found in (Kim et al., 2021a; Ohtori et al., 2004).

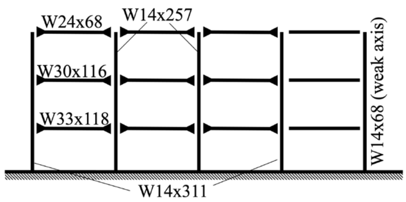

Figure 5. Configuration of the three-story steel building

- **Hazard model**

Hazard discerption is used twice in the analysis framework. The first is to get the site-specific IM distribution, $f_{IM}(im|H)$ used in Eqs. (10) and (11), and the second is to select/generate a site-specific events, e.g., ground motions, when estimating the reliability and redundancy curves. Recall that the main goal of the hazard analysis is to produce an explicit description of the distribution of future hazardous events considering various uncertainties. As such, the relationship between *IM* and its annual mean rate of occurrence is the main outcome of the hazard analysis, in general. *IM* could be either a scalar value or a combination of various *IMs* depending on the problem. For example, in the earthquake engineering field, spectral acceleration at the first mode period, $Sa(T_1)$, which shows a strong correlation with typical engineering demand parameters (EDP) is a widely used *IM*. Hazard analysis could be carried out probabilistically or deterministically, of which details are provided by many researchers (ASCE, 2019; Cornell, 1976; Kramer, 1996).

In the demonstration examples, we used the response spectrum estimated from a ground motion prediction equation (GMPE) by Boore & Atkinson (2008) as a design spectrum. The annual mean occurrence rate of the hazard, λ_H, is set to 10^{-3}. With a series of assumptions – unspecified fault type, moment magnitude 7, 30 km of the Joyner-Boore distance, and 700 m/s of the shear-wave velocity over the top 30 m – the seismic hazard curve for $Sa(T_1 = 1.01)$ and the PDF of $Sa(T_1 = 1.01)$ are respectively determined as shown in Figure 6(a) and (b). Note that the seismic hazard curve in Figure 6(a) is the multiplication of λ_H to the complementary cumulative distribution function (CCDF) of the PDF in Figure 6(b).

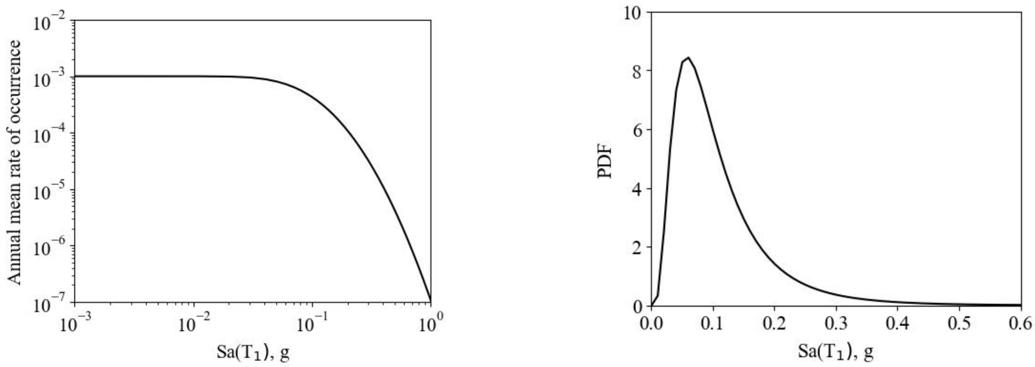

(a) Seismic hazard curve (b) Frequency function

Figure 6. Hazard curve and the corresponding hazard frequency function

- **Initial disruption scenarios**

In order to express the system failure probability in terms of β and π following Eqs. (3) and (14), it is important to ensure that the initial disruption scenarios $F_i, i = 1, 2, \dots, N_F$ are MECE events, in which N_F is the number of initial disruption scenarios. One may be tempted to select the initial disruption scenarios in terms of the failure of structural components, $C_i, i = 1,2, \dots, N_c$, where N_c is the number of components of interest, but such a set, in most cases (if not always), violates the MECE combination. To illustrate the difference between C_i and F_i, let us consider the three-story building model. The failure of i-th story weak column is considered as the component failure events of the building, C_i, $i = 1,2,3$. Figure 7 shows that C_1, C_2, and C_3 are not mutually exclusive due to the intersection of multiple events, e.g., joint failure of i-th and j-th stories.

Using the set theory, however, the MECE initial disruption scenarios can easily be defined in terms of the component failure events:

$$\boldsymbol{F} = \{F \mid F = (\cap_{i\in\mathbf{S}} C_i) \cap (\cap_{j\in\mathbf{S}^c} \bar{C}_j), \mathbf{S} \subset \{1, 2, \dots, N_c\}\} \quad (15)$$

where $\bar{C}_j$ denotes the survival of member j and $\mathbf{S^c}$ is the complement set of $\mathbf{S}$. For example, in the three-story building, $F_6 = \bar{C}_1 C_2 C_3$ (intersection notation ∩ is omitted here) represents 6-th disruption scenario of which 2nd and 3rd floors have failed ($\mathbf{S} = \{2, 3\}$) while the first floor has survived ($\mathbf{S^c} = \{1\}$). According to Eq. (15), the number of disruption scenarios increases exponentially as the number of components increases, i.e., $N_F = 2^{N_c}$. However, as will be discussed in Section 3, many scenarios in fact are significantly rare (i.e., extremely low $P(F_i|H)$) and can be disregard in the resilience analysis.

Note that the choice of components for defining the MECE is not unique and the number of MECE failure scenarios can be flexibly chosen based on engineering judgment and the computational costs. For instance, in the building example, it is possible to further divide weak columns or beams into several sections and treat these sections as individual components. This finer granularity allows for a more detailed analysis of the resilience performance of specific structural elements. It is remarked that, as mentioned in Section 2.2.2, the resilience threshold is adjusted based on the number of MECE events to minimize the effect of different MECE choices on the final evaluation of the structural resilience status.

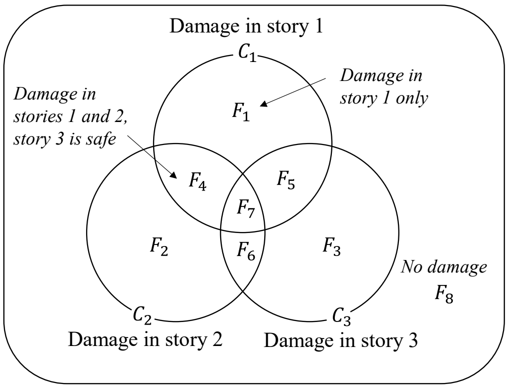

Figure 7. An example of MECE events (F) and non-MECE events (C) of the three-story building

- **Component-level limit-state**

A numerical definition of component failure is essential in obtaining the reliability curve in Eq. (10). Given that the disruption scenarios are defined as Eq. (15), the limit-state functions of each $F_i, i = 1, 2, \dots, N_F$ can be defined in terms of those of the component failure event $C_i, i = 1, 2, \dots, N_C$. For example, in the previous building model, the limit-state for the component failure can be established by excessive tensile stress at the weak column (rightmost column) of each story:

$$C_i = \{\sigma_{\mathrm{tr},i} - \sigma_i \le 0\}, \quad i = 1, \dots, 3 \quad (16)$$

where σ_i is the maximum tensile stress computed at i-th story's weak column, and $\sigma_{\mathrm{tr},i}$ is its maximum allowable threshold level. Using Eq. (16), the limit-state function of F_i is then defined as the joint occurrence of C_i and $\bar{C}_j$ as defined in Eq. (15). For the explanation purpose, in the three-story building, $\sigma_{\mathrm{tr},i} = 350$ Mpa is assumed. Estimated reliability curves $P(F_i|im, H)$ and indices β_i will be investigated in Section 3.

- **Component damage model and system-level limit-state**

The estimation of redundancy analysis starts by numerically modeling the degraded performance originating from the given disruption scenarios. Given the fact that the performance degradation stems from the component-level (or scenario-level) disruptions, one of the convenient options to represent the performance degradation is to replace the material properties, e.g., stiffness and strength, or geometric area with those of the damaged ones. Figure 8 shows an illustrative example in which the bilinear envelope (solid line) of the material model of the damaged weak columns is replaced by a new bilinear envelope (dashed line). The stiffness of the original material property, k_1, is reduced by multiplying α_E, while the yield strength F_y is reduced to $\alpha_y F_y$, in which $\alpha_E = 0.4$ and $\alpha_y = 0.2$ are used in this example following Li (2006). The degraded numerical model can describe the load redistribution initiated by the disruption scenario and properly represent the performance degradation of the structure.

In addition to the updated numerical model, a proper system-level limit-state needs to be defined to estimate the redundancy curve in Eq. (11). The system failure event in our example is defined in terms of the global response of the system following the common practice (ATC-58, 2012a, 2012b) given by

$$F_{sys} = \{\delta_{sys} - d_{roof,i} \leq 0\} \tag{17}$$

where δ_{sys} stands for the maximum allowable peak roof drift, and $d_{\mathrm{roof,i}}$ represents the peak roof drift of the structure obtained from the dynamic analysis with taking into account the initial disruption F_i . In our example, $\delta_{sys} = 0.07$ is assumed. Detailed procedures to estimate the redundancy curves will be addressed in Section 3.

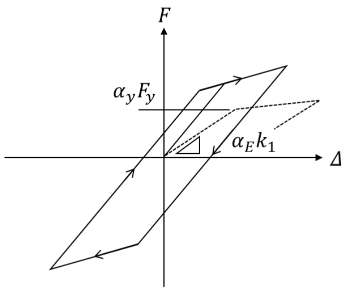

Figure 8. Properties of damaged components

- **Socioeconomic information**

Since recoverability stands for the ability to quickly respond to disaster impacts and rapidly recover the damaged structural components to the original state or the desired performance level, it should be determined not only as a direct repair cost but by a comprehensive analysis of the structure and social science aspects. Furthermore, the recoverability index should incorporate enough information to help engineers or stakeholders determine whether the structure needs to be retrofitted or not. Based on the desired properties, proper socioeconomic information is required to estimate recoverability. Many research efforts have been made to incorporate social science aspects in the recoverability index (Cimellaro et al., 2010; Didier et al., 2018; Liang & Xie, 2021), nevertheless no index is available to estimate the recoverability index for each initial disruption scenario. Thus, further study is currently underway to quantitatively define the recoverability index and investigate its relationship with the resilience limit-state.

3. Estimation of reliability and redundancy curves for each disruption scenario

The estimation of reliability and redundancy curves is the most computationally intensive step in the proposed resilience assessment framework. This section provides computationally efficient and practically feasible methods to estimate those curves. For the sake of notational brevity, we use the followings to represent the reliability and redundancy curves, respectively.

$$P_{\beta,i}(im) = P(F_i | im, H) \tag{18}$$

$$P_{\pi,i}(im) = P\left(F_{sys}\middle|F_i, im, H\right) \tag{19}$$

Unlike conventional fragility curves often defined as non-decreasing functions, the reliability curves typically have a non-monotonic shape because the initial disruption scenario F_i describes a mixed state of failed and survived components instead of only the failed components. In fact, the MECE condition of the initial disruption scenarios constrains the sum of the reliability curves to always be 1, regardless of im values. For instance, when $im = 0$, i.e., no external forces are applied to the structure, the probability of the "no components failure" scenario should be 1, while the other scenarios take the probability of zero. On the other hand, considering another extreme case where $im \to \infty$, only the "all components failure" scenario will have the probability of 1, which implies that the reliability curves of the other scenarios will decay to zero. In other words, all except these two special cases has skewed bell-shape curves along with IM. This implies that the reliability curves cannot (1) be assumed to have a simple functional form, such as a lognormal CDF, and (2) be calibrated independently for each F_i because of the constraint that all the reliability curves should sum up to 1.

After a high-level overview of the existing fragility analysis following Yi et al. (2022), three methods are proposed to estimate the reliability curves to consider the aforementioned characteristics, followed by a discussion on the redundancy analysis. To provide a comprehensive overview, we present Table 1 to summarize the computational aspects of the proposed three methods for estimating reliability curves. The methods are illustrated using the three-story building example.

Table 1. Summary of proposed methods to compute reliability curves

Method	**Subtraction method (Section 3.2.1)**	**Multinomial logistic regression (Section 3.2.2)**	**Screening of *force majeure* scenarios (Section 3.2.3)**
Purpose	To obtain reliability curves $P_{\beta,i}(im)$ in Eq. (18)		To screen out trivial (*force majeure*) scenarios that can be disregarded in β-π analysis
Strategy	Recursive subtraction of joint components failure fragility curves ($P(C_S\|im)$)	Multinomial classification using logistic regression model	Inspect the lower bound of β_i to find F_i of which the resilience requirement is satisfied with a large margin
Assumptions	Fragility curves of joint components failure ($P(C_S\|im)$) can be obtained by regular fragility analysis, e.g., under log-normal assumption.	Reliability curves follow the membership probability of the logistic regression model	No assumption
Definition	Eq. (28), where $P_{\beta,i}(im) = P\left(C_{S_i\bar{S}_i^c}\|im\right)$	Eq. (35) and (36)	F_i that satisfies Eq. (38) is trivial (*force majeure*)
Pros	Conventional fragility analysis methods (Section 3.1) can be utilized	All reliability curves are obtained as a single regression model	-
Cons	Errors in estimation can accumulate during the subtraction process	MLE optimization is needed	-

3.1. High-level overview of fragility analysis methods

The fragility curve is defined as the conditional failure probability given IM of a hazard:

$$P_f(im) = P(DS = 1|im) \tag{20}$$

where DS is a binary damage state index that takes one if the component or system is damaged, and zero otherwise. In practice, DS is represented as the demand being greater than capacity, i.e.,

$$DS = \mathbb{I}\{\delta_c - d \leq 0\} \tag{21}$$

where $\mathbb{I}(\cdot)$ is an indicator function, δ_c represents the response threshold (capacity), and d stands for the response of the component/system due to hazard loads (demand), which is often referred to as an engineering demand parameter. Among various fragility analysis methods, incremental dynamic analysis (IDA), cloud analysis, maximum likelihood estimation of the binary classification model, and extended fragility analysis are summarized in the subsequent paragraphs.

IDA gained popularity in light of intuitive analysis steps and the easiness of calibrating the parameters of a fragility function (Vamvatsikos & Cornell, 2002). IDA creates multiple splines on $\{im, d\}$ space, each obtained by running multiple dynamic structural analyses for varying scales of ground motion time histories. The uncertainty in the capacity of the system is represented in terms of IM values at which the splines cross the response threshold δ_c. The fragility curve of typical IDA procedure takes the form of lognormal CDF

$$P_f(im) = \Phi\left(-\frac{\theta - \ln im}{\beta}\right) \tag{22}$$

The parameters θ and β are respectively log-mean and log-standard deviation of the collected IM capacity samples during the IDA analysis.

The cloud analysis predicts the mean response by introducing the power law assumption between IM and d (Cornell et al., 2002)

$$E[\ln d] = a + b \ln im + \varepsilon \tag{23}$$

where ε follows a normal distribution, whose mean is zero and the standard deviation is σ, i.e., $N(0, \sigma^2)$. By minimizing the squared error of the linear regression under homoscedasticity assumption, $\{a, b, \sigma\}$ are estimated. Using the estimated parameters, the following fragility curve is obtained.

$$P_f(im) = \Phi\left(-\frac{\ln \delta_c - \ln d}{\sigma}\right) \tag{24}$$

Next, a method by Shinozuka et al. (2000) treats the fragility analysis as a binary classification task. Using the lognormal CDF in Eq. (22) as the form of the fragility function, parameters θ and β are obtained by maximizing the following Bernoulli likelihood function

$$L = \prod_{n=1}^{N_{sample}} P_f\left(im^{(n)}\right)^{DS^{(n)}} \left(1 - P_f\left(im^{(n)}\right)\right)^{1-DS^{(n)}} \tag{25}$$

where N_{sample} represents the number of samples obtained from dynamic analyses, and the superscript (n) stands for the n-th analysis data. Once θ and β are calibrated, the fragility can be described using Eq. (22).

Lastly, as an alternative to the lognormal CDF, a log-logistic distribution is used as a fragility function in the extended fragility analysis method (Andriotis & Papakonstantinou, 2018)

$$P_f(im) = \frac{1}{1 + \exp -(\alpha_o + \alpha_1 \ln im)} \tag{26}$$

where α_o and α_1 are coefficients calculated again by maximizing Eq.(25). A merit of introducing the Bernoulli likelihood function is that the parameters of the fragility function are estimated in terms of DS instead of the actual response quantity d. This is useful particularly when the system failure is defined as a combination of multiple response quantities, e.g.,

$$DS = \mathbb{I}\left\{\cap_{i=1}^{N_c} (\delta_i - d_i \leq 0)\right\} \tag{27}$$

3.2. Estimation of the reliability curves

3.2.1. Method 1: Subtraction method

To address the challenges discussed in the beginning of Section 3, a new method termed the "subtraction method" is introduced. This method allows us to apply conventional fragility methods for the reliability tasks by drawing a relationship between the probability of $F_i, i = 1, 2, \ldots, N_F$ and those of joint $C_i, i = 1,2, \ldots, N_c$ in Eq. (15). For an initial disruption scenario $F_i = C_{\boldsymbol{S}\bar{\boldsymbol{S}}^c}$, the reliability curve can be reformulated using the subtraction method as

$$P(C_{S\bar{S}^c}|im) = P(C_S|im) - \sum_{j \in S^c} P(C_S C_j|im) + \sum_{(j<k)\text{ for } j,k \in S^c} P(C_S C_{jk}|im) - \cdots + (-1)^{N_{S^c}} P(C_{SS^c}|im) \quad (28)$$

in which

$$C_{S\bar{S}^c} = (\cap_{i \in S} C_i) \cap (\cap_{j \in S^c} \bar{C}_j), \qquad S \subset \{1,2,3,\ldots,N_c\} \quad (29)$$

and

$$C_S = (\cap_{i \in S} C_i), \qquad S \subset \{1,2,3,\ldots,N_c\} \quad (30)$$

where N_{S^c} is the number of elements in $\boldsymbol{S}^c$. The subtraction method converts the task of the reliability curve estimation (lefthand side term of Eq. (28)) to the fragility analysis of joint component failures (righthand side terms of Eq. (28)). Thereby, no care needs to be made to consider the constraints discussed previously. Since these joint component failures do not condition on survival events, $\bar{C}_j$ in Eq. (28), the conventional fragility analysis methods, e.g., under lognormal assumption, can be adopted in the reliability analysis.

For example, in the three-story building example, we can represent the reliability curve of $F_1 = C_{1\bar{2}\bar{3}}$ using Eq. (28) as follows:

$$P(F_1|im) = P(C_{1\bar{2}\bar{3}}|im) = P(C_1|im) - P(C_{12}|im) - P(C_{13}|im) + P(C_{123}|im) \quad (31)$$

In the same manner as above, the followings are the expressions of other MECE events using the subtraction method

$$\begin{aligned} P(F_4|im) &= P(C_{12\bar{3}}|im) = P(C_{12}|im) - P(C_{123}|im) \\ P(F_5|im) &= P(C_{1\bar{2}3}|im) = P(C_{13}|im) - P(C_{123}|im) \\ P(F_7|im) &= P(C_{123}|im) \end{aligned} \quad (32)$$

A graphical illustration of the subtraction method used in the three-story building example is shown in Figure 9. The following is the summary of the procedure when applying the subtraction method to the three-story budling.

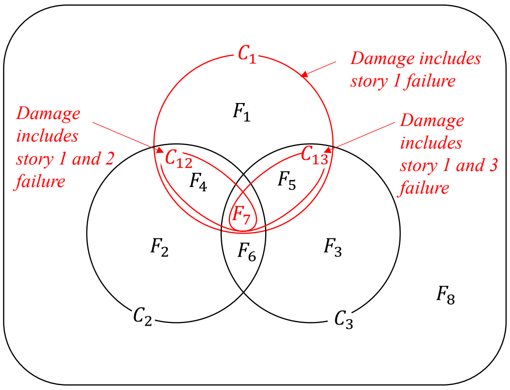

Figure 9. MECE events (F) and their supersets (red) of the three-story building example

Procedure

1. Estimate reliability curves of each joint component failure events C_{S_i}, $\boldsymbol{S}_i \subset \{1,2,3\}$ using fragility analysis methods described in Section 3.1. The Bernoulli model-based fragility method is used in this example.
    i. Collect/generate the multiple ground motion time histories for a specific region of interest, and run structural dynamic analysis to collect a cloud of data samples $\left\{im^{(n)}, z_1^{(n)}, z_2^{(n)}, \ldots, z_{N_F}^{(n)}\right\}$, $n = 1, \ldots, N_{sim}$, where $N_{sim} = 50$ is the total number of model evaluations, $N_F = 2^{N_c} = 8$, and z_i is the binary occurrence index that takes 1 if C_{S_i} has occurred, and 0 otherwise.
    ii. For $i = 1, \ldots, N_F$, using $\left\{im^{(n)}, z_i^{(n)}\right\}$, calibrate the fragility function parameters in Eq. (22) by maximizing the likelihood defined in Eq. (25) to obtain the fragility curves $P(C_{S_i}|im)$.
2. Calculate the reliability curves of $F_i = C_{S_i\bar{S}_i^c}$ using Eq. (28), i.e., $P_{\beta,i}(im) = P\left(C_{S_i\bar{S}_i^c}|im\right)$.

Figure 10 describes the estimated reliability curve using the above procedure. A total of 50 ground motions are used in the dynamic analysis which are spectrum-matched or spectrum-compatible to a design spectrum presented in Section 2.3 (See Figure 14(b)). The ground motion time histories are selected from the NGA-West database (Power et al., 2008). It is remarked that one may get a negative $P_{\beta,i}(im)$ using the subtraction method. To the authors' observation, the effect of negativity was not significant as it was apparent only at the improbable range of hazard magnitude, e.g., beyond 4g in the numerical example, where g is the gravitational acceleration. Thus, we decided to enforce the negative values to zero in the calculation. However, it is possible to strictly prevent the negative probability density by applying a constraint such that a single dispersion parameter, β in Eq.(22), is assigned to all $P(C_{S_i}|im)$, i.e., $\beta_1 = \beta_2 = \cdots = \beta_{N_F} = \beta$. In other words, only the median parameters θ_j and β are optimized during the maximum likelihood estimation. Note that similar tricks are often introduced in the traditional fragility analysis to prevent crossings between multiple damage states, for example, as used in Shinozuka et al. (2003).

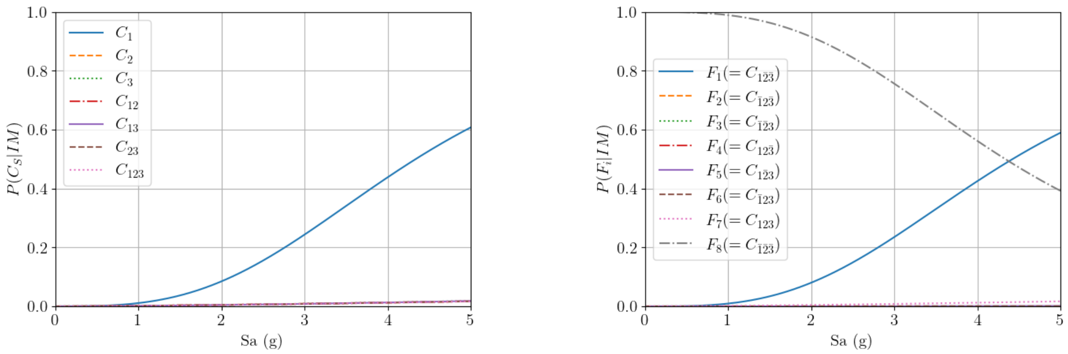

(a) Fragility curves for C_s (b) Reliability curves for the MECE events

Figure 10. Reliability curves using the subtraction method

Furthermore, an approximation approach is proposed to facilitate the efficient estimation of the joint component fragility function $P(C_S|im)$ (and all the lefthand side terms in Eq. (28)) using the fragility functions of the single components $P(C_i|im), i \in \boldsymbol{S}$, and their correlation information. By substituting the component failure definition in Eq. (21) into Eq. (30) after applying the natural logarithm, the joint component failure is written as a series system reliability problem

$$P(C_S|im) = P(\cap_{i\in S} C_i|im) = P(\cap_{i\in S} \{\log(\delta_{ci}) - \log(d_i) \leq 0\}|im) \quad (33)$$

Assuming that $\log(d_i)$ are joint normal distribution, the below can be derived (Der Kiureghian, 2005; Hohenbichler and Rackwitz, 1983)

$$P(C_S|im) = \Phi_m(-\boldsymbol{\beta}(im); \boldsymbol{R}(im)) \quad (34)$$

where $\Phi_m(\cdot; \boldsymbol{R}(im))$ is the m-dimensional multivariate standard Gaussian CDF with correlation matrix of $\boldsymbol{R}(im)$, $\boldsymbol{\beta}(im)$ is a vector of reliability indices whose element is defined as $\beta_i = \Phi^{-1}(P(C_i|im))$, and $\boldsymbol{R}(im)$ is constructed by the inner product of the normalized negative gradient vector of each components' limit-state function at the design point. Using Eq. (33) and $P(C_i|im)$, $P(C_S|im)$ can be approximated with a small computational cost, which facilitates the efficient computation of the subtraction method. However, one should be cautious about the fact that it relies on the normality assumption because this error can be accumulated in the calculation of Eq. (28). Therefore, for example, one may want to perform a goodness-of-fit test to measure how well $\log(d_i)$ follows the joint normal distribution. This effect of error accumulation is alleviated when the scenario screening, which will be discussed in Section 3.2.3, is introduced.

3.2.2. Method 2: Multinomial logistic regression

Alternatively, the task of estimating reliability curves can be formulated into a multi-class classification problem of which the input is IM and the categorical outcomes are F_i. Then the membership probability, i.e., the probability that a given sample belongs to a particular category, is in nature equivalent to the definition of reliability curve. In particular, the membership probability of the logistic regression model takes the form of (Long & Freese, 2006)

$$P_{\beta,i}(im) = \frac{\exp(b_{oi} + b_i \ln im)}{1 + \sum_{j=1}^{N_F-1} \exp\left(b_{oj} + b_j \ln im\right)} \tag{35}$$

for $i = 1, \ldots, N_F - 1$, and

$$P_{\beta,N_F}(im) = \frac{1}{1 + \sum_{j=1}^{N_F-1} \exp\left(b_{oj} + b_j \ln im\right)} \tag{36}$$

Therefore, the formulation naturally satisfies $\sum_{i=1}^{N_F} P_{\beta,i}(im) = 1$. The coefficients b_{oi} and b_{1i} are calibrated by maximizing the following likelihood function

$$L\left(\{b_{oi}, b_{1i}\} \middle| \{im^{(n)}, z^{(n)}\}\right) = \prod_{n=1}^{N_{sample}} \prod_{i=1}^{N_F} P_{\beta,i}\left(im^{(n)}\right)^{\mathbb{I}(z^{(n)}=i)} \tag{37}$$

where $z^{(n)}$ is the n-th sample of the categorical outcome as the index of the disruption scenario. Once $\{b_{oi}, b_{1i}\}$ for $i = 1, \ldots, N_F - 1$ are obtained by maximizing the likelihood function of Eq. (37), the reliability curve for $i = N_F$ can be automatically determined from Eq. (36). A merit of this procedure is that the reliability curves for all disruption scenarios are obtained simultaneously with attaining the condition $\sum_{i=1}^{N_F} P_{\beta,i}(im) = 1$. The following is the application of the multinomial logistic regression to estimate the reliability curves of the three-story building.

Procedure

1. Perform structural dynamic analysis using a set of ground motions to obtain a cloud of data samples $\{im^{(n)}, \mathrm{z}^{(n)}\}$, $n = 1, \ldots, N_{sim}$, where $N_{sim} = 50$.
2. Find $\{b_{oi},\ b_i\}$, where $i = 1, \ldots, 7$, by maximizing the likelihood function in Eq. (37).
3. Following the definition, the reliability curves are equivalent to the calibrated logistic regression model in Eqs. (35) and (36).

Figure 11 shows the results of the reliability curve estimated using the multinomial logistic regression. As shown in Figure 11(a), the summation of $P_{\beta,i}(im)$ for all MECE events is always 1 for every *IM*. Figure 11(b) plots the reliability curves of each MECE event, which shows a good agreement with the results using the subtraction method in Figure 10(b). Note that F_2, F_3, and F_6 are not observed in the dataset $\{\mathrm{z}^{(n)}\}$, thus assumed to have zero probability. The underlying assumption is that the reliability indices of those scenarios are smaller than those observed. Therefore, if deemed needed, one needs to revisit this assumption, and run more simulations to make sure all the critical cases are taken into account in the resilience assessment. The additional simulations are not needed if at least one scenario in the β−π diagram satisfies the screening condition that will be discussed in Section 3.2.3.

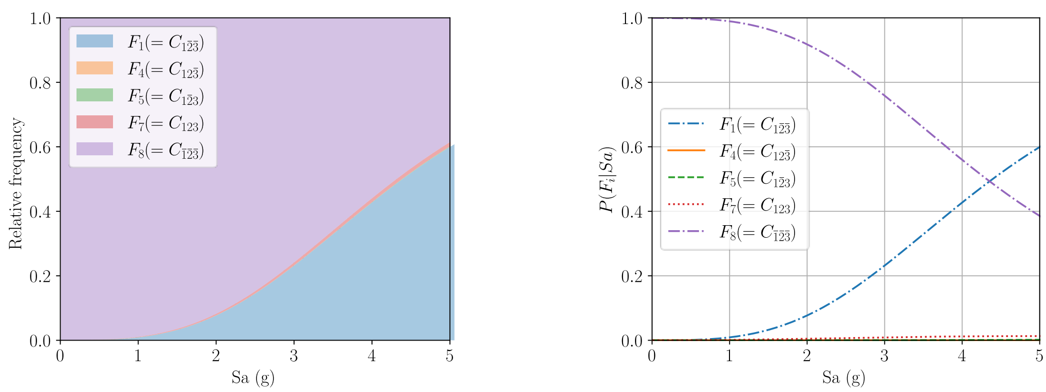

(a) Participation of MECE events along with IM (b) Reliability curves for MECE events

Figure 11. Reliability curves obtained by multinomial logistic regression

3.2.3. Method 3: Screening of force majeure scenarios

One critical challenge in the resilience assessment is that the number of initial disruption scenarios increases exponentially as that of the structural components increases. Since the previously introduced methods should check whether the reliability index satisfies the resilience limit-state for every MECE event, it is still limited to applying the reliability-based resilience assessment framework to a structure having a large number of structural components such as a cable-stayed bridge. However, since there are lots of *force majeure* MECE events, which have extremely small occurrence probability, the screening method can exclude those from the resilience analysis.

In particular, for a scenario of $F_i \subset C_S$, if one can show that the below is satisfied

$$P(C_S|H)\Phi(-\pi_i) < P_{dm}/(\lambda_H N_F) \tag{38}$$

no more reliability analysis is required for F_i because F_i will always satisfy the resilience threshold in Eq. (5) ($P(F_i|H) = \Phi(-\beta_i) < P(C_S|H)$ always holds). For instance, in Figure 9, if the failure probability of C_1 satisfies the resilience performance threshold of Eq. (38), we can infer that F_1, F_4, F_5, and F_7 (or $C_{1\bar{2}\bar{3}}, C_{12\bar{3}}, C_{1\bar{2}3}$, and C_{123}, respectively) meet the disaster resilience goal without further analysis. Similarly, if C_{23} satisfies the resilience limit-state, the analysis of F_7 and F_6 (C_{123} and $C_{\bar{1}23}$) can be disregarded in the resilience analysis. Using this property, it is possible to drastically reduce the number of MECE events considered in the resilience assessment framework. Moreover, the screening method enables not only to efficiently assess the resilience performance of the existing structures but also to quickly check whether a candidate structure is within the resilience-safe domain with the β–π–γ diagram during the design phase.

3.3. Estimation of the redundancy curves

The redundancy curve in Eq. (19) can be straightforwardly obtained from a fragility analysis described in Section 3.1 after considering the component damage scenarios in the numerical model. In the analysis, the same stochastic excitation set used in the reliability analysis is employed. As already discussed in Lim et al. (2022), the *force majeure* scenarios with sufficiently low occurrence probability can be omitted in the redundancy analysis. For example, if

$$\Phi(-\beta_i) < P_{dm}/(\lambda_H N_F) \tag{39}$$

is satisfied, Eq. (14) is already satisfied for the scenario F_i regardless of the redundancy index π_i. Furthermore, by extending the discussion in Section 3.2.3, it can be shown that if

$$P(C_S|H) < P_{dm}/(\lambda_H N_F) \tag{40}$$

is satisfied, any reliability and redundancy analyses associated with all $F_i \subset C_S$ can be omitted. A procedure to estimate the redundancy curves for the three-story building example is provided in the following.

Procedure

Repeat below for $i = 1, \ldots, 8$:

1. If Eq. (39) or Eq. (40) is satisfied, label F_i as safe and exclude F_i from further analysis. In other words, neglect Steps 2 and 3 and move on to $i + 1$, else move on to Step 2.
2. Update the structural model in accordance with the damage scenario F_i.
3. Perform fragility analysis with a predefined system-level limit-state using the damaged structure to obtain $P_{\pi,i}(im)$

Figure 12(a) provides an example of the IDA results to evaluate the system performance given $F_1 = C_{1\bar{2}\bar{3}}$ (failure of the first story only), while Figure 12(b) illustrates the estimated redundancy curves. Note that among the failure scenarios, F_1, F_4, F_5, F_7, and F_8 are inspected in accordance with the discussion in Section 3.2.2. By comparing the curves of F_8 and F_7, one can notice that, in this example, only a minor performance decay is observed even when many components failed, indicating that the component damages do not in fact have a critical influence on the global structural response. This is attributed to the assumption of the damage model we introduced. A summary of the reliability and redundancy analyses is presented in Table 2 with the traditional fragility analysis in performance-based engineering.

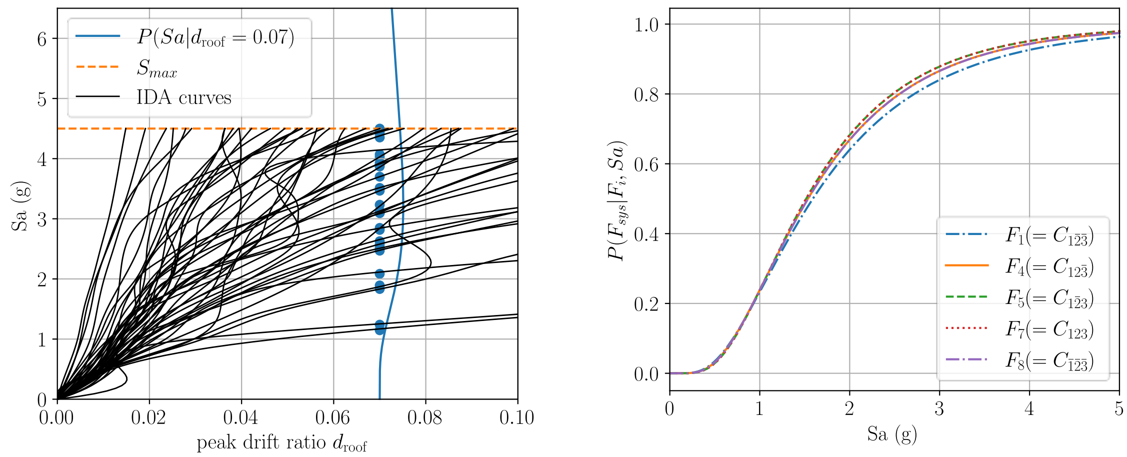

(a) IDA results of F_1 (b) Redundancy curves

Figure 12. Results of the redundancy analysis

Table 2. Summary of reliability and redundancy curves in comparison with traditional fragility curves

Category	Performance-based Engineering	Resilience-based Engineering	
Step	**Fragility analysis**	**Reliability analysis**	**Redundancy analysis**
Definition*	$P_f(im) = P(DS = 1\|im)$ Eq. (20)	$P_{\beta,i}(im) = P(F_i\|im)$ Eq. (18)	$P_{\pi,i}(im) = P(F_{\text{sys}}\|F_i, im)$ Eq. (19)
Failure limit-state	Component- or system- level failure	Component-level failures corresponding to initial disruption scenario F_i	System-level failure
System status before the analysis	No damage	No damage	Joint components damages corresponding to initial disruption scenario F_i
Methods	IDA, multiple strip analysis (MSA), extend fragility method, etc.	Subtraction method, multinomial logistic regression	IDA, MSA, extend fragility method, etc.
Hazard types	Dynamic excitations with high aleatory uncertainty (i.e., stochastic excitations)		

* H in the conditioning term is omitted following the convention in fragility analysis

4. Numerical Investigations

The proposed seismic resilience assessment framework is demonstrated using a mid-rise building and a bridge model. For the reliability analysis, the multinomial logistic regression method (Section 3.2.2) and screening approach (Section 3.2.3) are respectively applied in the examples.

4.1. Nine-story building

4.1.1. Target structure and hazard

The first example considers a benchmark nine-story building model shown in Figure 13 adopted from the SAC Phase II Steel project report. This building is designed to meet the design standard of the mid-rise building located in Los Angeles, California, region. The model has a basement level as shown in Figure 13, and the horizontal displacement at the ground level is restrained to be zero. The building is modeled using OpenSees (McKenna, 2011) using bilinear material model (Steel 01) for both beams and columns, and the Rayleigh damping with damping ratio of 0.03 is introduced. The first mode period of the structure is $T_1 = 2.27$s. The hazard description in Section 2.3 is employed, which is characterized by the PDF of spectral acceleration $Sa(T_1 = 2.27)$ shown in Figure 14(a). Moreover, a set of spectrum-compatible 50 ground motion time histories is shown in Figure 14(b).

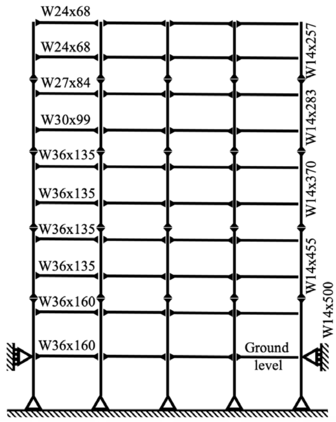

Figure 13. Nine-story Steel building model

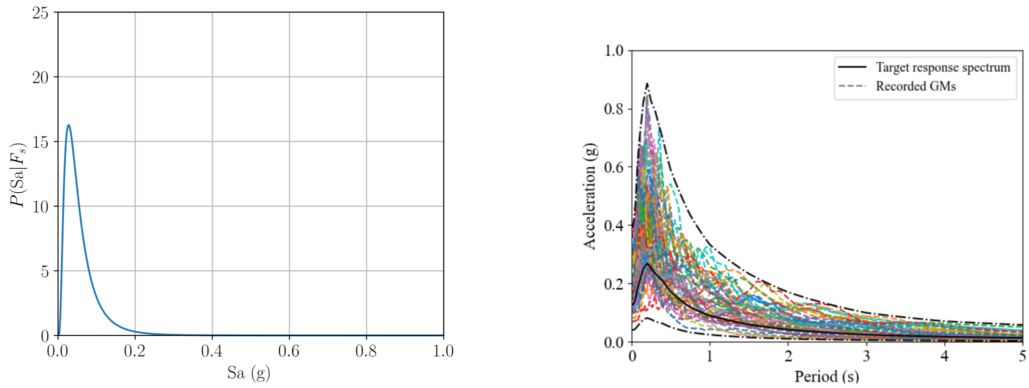

(a) Frequency function (b) Response spectrum of the ground motions

Figure 14. Hazard description

4.1.2. Initial disruption scenarios and limit-states

The component failure events are defined as an occurrence of an excessive drift ratio at each story:

$$C_i = \{\delta_i - d_i \leq 0\}, \quad i = 0, \ldots, 9 \tag{41}$$

where d_i is the peak inter-story drift ratio at the i-th story and $\delta_i = 0.02$ is its maximum allowable threshold. Note that the response at the basement level is indexed with $i = 0$. The ten components lead to 1024 (2^{10}) initial disruption scenarios. The system-level limit-state is represented in terms of the maximum roof drift ratio as in Eq. (17) with $\delta_{sys} = 0.07$.

4.1.3. Resilience performance

Using 50 ground motions with different scaling factors, a total of 485 simulations are performed, and 84 among possible 1,024 scenarios are observed. The framework assumes that only 84 scenarios are plausible, while other scenarios are considered to have an occurrence probability (near) zero. The 485 data points are used to estimate the logistic regression parameters in Eq. (35), and the results are shown in Figure 15. Figure 15(a) and Figure 15(b) are equivalent figures that show the probability of the system lying in a certain initial disruption scenario given IM, where the significant scenarios are labeled as "C$\boldsymbol{S}$" meaning that members in $\boldsymbol{S}$ fail while all the other members are safe, i.e., equivalent to $C_{\boldsymbol{S}\bar{\boldsymbol{S}}^c}$ in Eq. (29). As expected, the probabilities of all MECE events always sum up to one because of the MECE condition. The figure shows that the probability of a "no component failure" case decreases as the IM increases. In the range of high IM values, the event of C1-9 (all components except for the basement level failure) dominates the response followed by C1-8 (all components except for the basement and the top story failure). Figure 15(c) and Figure 15(d) summarize the results in terms of the number of failed components. Among different cases, the "no component failure" case dominates under relatively small IM values, but the increase has been observed for the probability of "8 to 10 components failure" cases as IM increases.

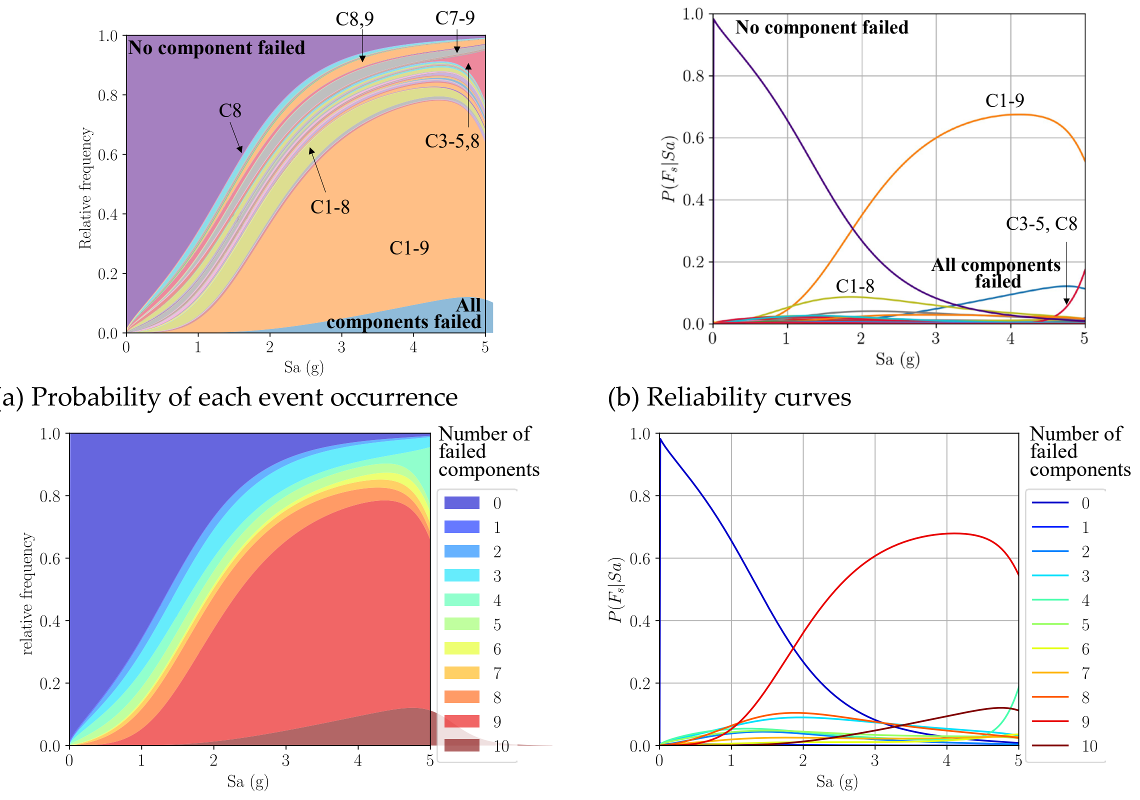

(a) Probability of each event occurrence (b) Reliability curves

(c) Summarized probability of event occurrence (d) Summarized reliability curves

Figure 15. Reliability curves of nine-story building ("C***S***" represents the failure of components in ***S*** and survival of all the other components)

The redundancy analysis is performed for the 84 scenarios and the results are presented in Figure 16. It is shown in Figure 16(a) that the most critical scenarios in terms of redundancy curves are the "all components failure" case and C0-8. On the other hand, the "no component failure" case and several scenarios with a few members failure cases such as C3 and C8 appear to be relatively redundant, which agrees well with the general intuition - a larger number of remaining load-resisting members leads to a higher redundancy. Meanwhile, the updated distribution of IM (as defined in Eq.(8)) used for redundancy analysis is presented in Figure 16(b) and the scenarios with the five largest and five smallest mean IM of the updated distribution are listed in Table 3, where $E[\cdot]$ represents the mathematical expectation. It can be seen that different scenarios lead to various ranges of updated IM.

Table 3. Mean of IM conditioned on each disruption scenario

Largest		Smallest	
Disruption scenarios ($\boldsymbol{F_s}$)	**E[$\boldsymbol{Sa \mid F_s}$]**	**Disruption scenarios ($\boldsymbol{F_s}$)**	**E[$\boldsymbol{Sa \mid F_s}$]**
C3	0.048	C3-5,8	5.60
No Component failed	0.056	C1,2,4-9	5.41
C2,3,7,8	0.060	C1,2,4,5,7-9	3.95
C2-6,8	0.061	C1,4,5,7-9	3.12
C2-5,7-9	0.063	C1-4,8,9	2.71

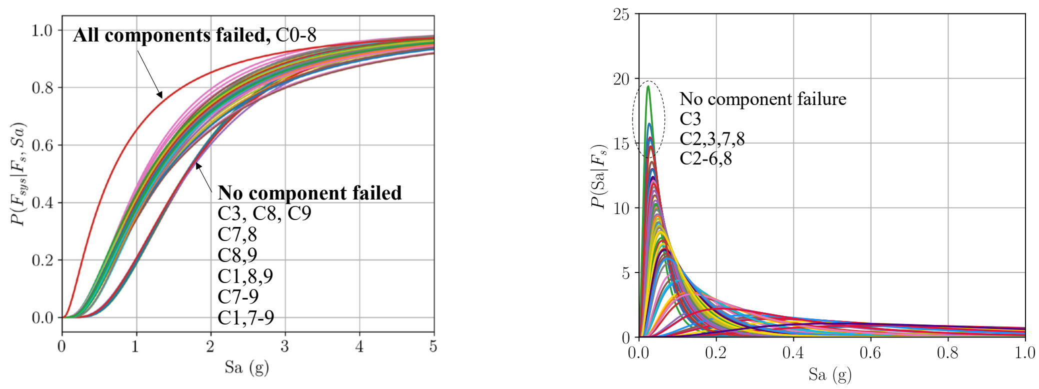

(a) Redundancy curves (b) Updated distribution of IM

Figure 16. Redundancy curves of the nine-story building ("C***S***" represents the failure of components in ***S*** and survival of all the other components)

The β–π diagram is shown in Figure 17(a). The color represents the number of failed components, which can be used as a recoverability indicator. From the decaying trend of the scatter plot, one can draw insight into the complementary nature of the reliability and redundancy across the scenarios. The event C1,2,4-9, for example, has high reliability (i.e., it is rare to have the combination of components 1,2,4-9 failed) and low redundancy (i.e., the failure of the components 1,2,4-9 is associated with high IM values as shown in Table 3, which is likely to trigger the progressive system failure). On the contrary, C3 has a low reliability but a high redundancy level.

To investigate the effect of IM updating in the redundancy assessment, the β–π diagram without updating the IM (i.e., using Eq. (12)) is presented in Figure 17(b). While the reliability indices remain the same as Figure 17(a), the redundancy characteristics are significantly different from those with updating. In this case, π directly follows the trend observed in the redundancy curves in Figure 16(a). Meanwhile, the reason that some single-member failures have higher reliability than multiple-member failures can be explained by the high correlation between the member failure events. In other words, it is likely to have multiple member failures than only a single member failure in this example.

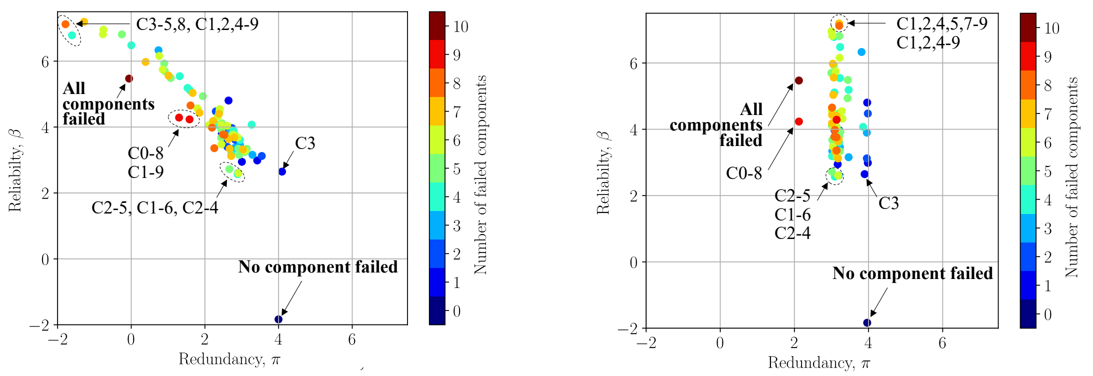

(a) With updating of intensity measure distribution (b) Without updating of intensity measure distribution

Figure 17. β–π diagram of the nine-story building structure

4.2. Cable-stayed bridge

4.2.1. Target struture

A cable-stayed bridge is introduced to attest to the applicability and effectiveness of the proposed framework to a more complex civil structure. A nonlinear three-dimensional finite element model is constructed using OpenSees (McKenna, 2011) as shown in Figure 18. The bridge consists of 2 pylons, girder, and 128 cable elements, and its total length is 1,069 m. Note that no soil-structure interaction is considered in this study.

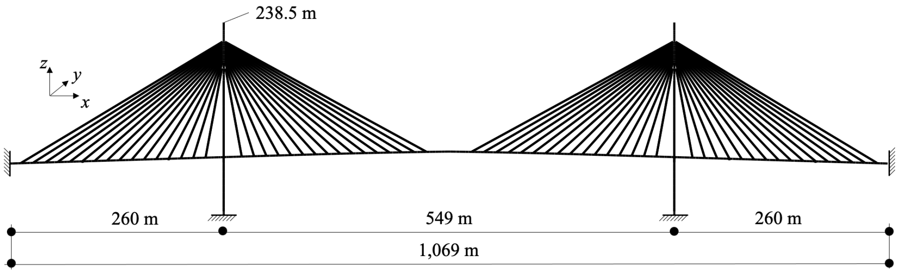

Figure 18. Configuration of the example structural system

A bilinear tension-only material with a yield stress of 1,770 MPa and 1% of the post-yield stiffness ratio is introduced to model the cable elements. The sagging of each cable element is considered from Ernst (1965) with Young's modulus of the cable strand of 195 GPa. The initial tension force of the cable element is converted to the initial strain in the truss model. On the other hand, linear elastic frame elements are employed to model the girder and pylons. In addition, linear springs are used to model the bridge bearings for simplicity. Because no nonlinear element except the cables is introduced in the numerical model, a limitation exists in describing the local collapse of structural elements and seismic behaviors after the yield point. The damping ratio of 3% is assumed based on the literature (Kim et al., 2021b; Tang et al., 2008; Zhong et al., 2017).

Dynamic characteristics of the numerical model are investigated by performing the eigenvalue analysis. The estimated modal periods are tabulated in Table 4, while Figure 19 illustrates the corresponding mode shapes. Note that the eigenvalue analysis is performed after applying the dead load and pretension force of the cables.

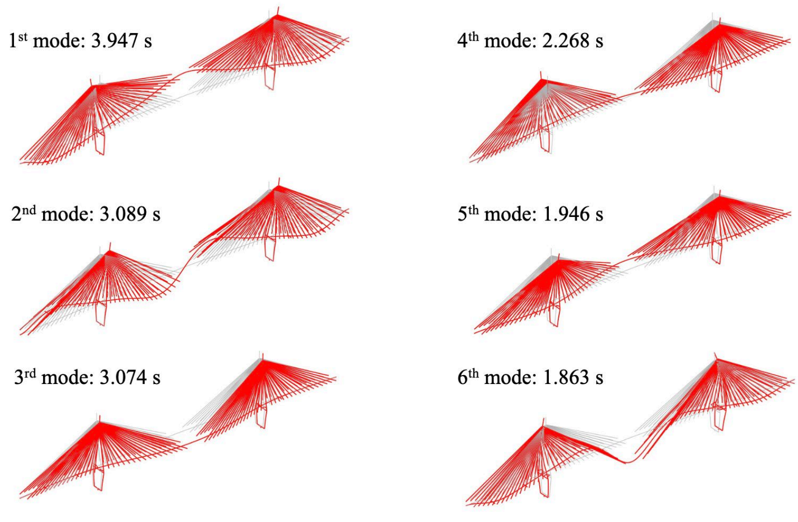

Figure 19. Modal shapes of the long-span bridge

Table 4. Modal periods of the cable-stayed bridge

Mode	1	2	3	4	5	6
Period (s)	3.947	3.089	3.074	2.268	1.946	1.863

4.2.2. Hazard analysis

In the same manner as the three- and nine-story building examples, we assume a point source earthquake event with moment magnitude of $M = 7$. The distance between the epicenter and the cable-stayed bridge and the shear wave velocity are set as 20 km and 750 m/s, respectively. Under these assumptions, the PDF of the IM given the hazard is obtained by using the GMPE by Boore and Atkinson (2008).

4.2.3. Initial disruption scenarios and limit-states

Among various system damage scenarios, this study considers those induced by initial cable disruptions, as the cable elements are the main medium of the load transfer from the superstructure to the pylon. Note that while other structural elements or combinations of various structural elements could be selected to define the initial disruption scenarios, this study only employs the cable elements for the purpose of explaining the proposed framework. The limit-state of the cable elements used to derive reliability curves, $P_{\beta,i}(im)$, is defined as the seismic demand exceeding 50% of the yield stress (i.e., 885 MPa). Since there are 128 cable elements in the model, the total number of MECE initial disruption scenarios is 2^{128}, including the "no element failure" scenario.

Since the cable-stayed bridge in the system-level has multiple failure modes, the system failure limit-state function, in this research, is defined as the presence of at least one failure mode. Thus, the redundancy analysis is considered as a series system reliability problem following the approach summarized by Der Kiureghian, 2005. Based on the literature survey (Nielson & DesRoches, 2007; Padgett & DesRoches, 2008; Pang et al., 2014; Yi et al., 2007), four critical system failure scenarios are identified, and the corresponding limit-states are summarized in Table 5. When computing the redundancy curves, $P_{\pi,i}(im)$, dynamic analyses are conducted after removing the failed cable elements of the bridge.

Table 5. System-level limit-states of the cable-stayed bridge

Components	Engineering demand parameter (EDP)	Limit-states
Pylon	PM safety factor (Kim et al., 2021b)	<0
Pylon	Ratio of the peak displacement of pylon to the height of pylon	>1%
Girder	Ratio of the peak transverse displacement of girder to the length of girder	>1%
Cable	Cable tension force	>885 Mpa

4.2.4. Resilience performance

As discussed earlier, a huge number of structural components in the cable-stayed bridge may result in numerous initial disruption scenarios. However, it may not be necessary to evaluate all the reliability and redundancy indices for each scenario, if many scenarios conservatively satisfy the resilience threshold as discussed in Sections 3.2.3 and 3.3. In this example, we illustrate a case where it is sufficient to assess the resilience performance for individual component failure events instead of all initial disruption scenarios. In other words, as described in Section 3.2.3, a set of β and π is first estimated for C_i (128 cases) and is shown that we do not need to estimate them for all F_i (2^{128} cases) because they are guaranteed to be safe. However, note that if some scenarios do not secure the resilience criteria, further steps are needed to estimate β and π for initial disruption scenarios F_i.

To test the applicability of the proposed framework to general stochastic excitations, spectrum-compatible, bi-directional artificial ground motions are generated by following an algorithm and parameter sets provided in Kim et al. (2021). Although the algorithm enables to simulate multi-variate ground motions, in this research, the same set of orthogonal ground motion time histories is used for each support. By assuming the mean of a response spectrum obtained using the assumptions in Section 4.2.2 as the target spectrum, 30 sets of ground motion time histories are generated. When generating the spectrum-compatible orthogonal ground motion time histories, we scale the target spectrum to capture the seismic behavior of the structural system for a broad range of ground motion intensities. 30 different scale factors are introduced to make peak ground acceleration (PGA) of the target spectrum ranging from 0.16 g to 1.0 g. Using the cloud analysis in Section3.1, both the reliability and redundancy curves are estimated for the component failure scenarios. The scalar IM is established as the geometric mean of PGA of the two orthogonal ground motions.

Figure 20 shows the β−π diagram of 32 component failure cases with the resilience limit-state surface corresponding to $P_{dm}/(\lambda_H N_F) = 10^{-4}$. Note that because of the bidirectional symmetry of the bridge system, only a quarter of the elements are considered. In the figure, we disregard the component failure scenario having a reliability index greater than 12, which is considered as *force majeure*. Because all the β values already exceed the resilience criterion, no redundancy analysis is required. However, for visualization purposes, the redundancy is evaluated where the conditioning scenario is "every component survives but member *i*." As shown in the figure, even though we conservatively assess the reliability performance of the bridge, all cases of the β−π are located outside the resilience limit-state surface (i.e., satisfy the socially-accepted criteria). The estimated reliability and redundancy values are well-matched with the characteristics of the cable bridge, in that scatter points indicated by blue solid and red dashed boxes in Figure 20 are respectively the failure scenario of the first and second outermost cables in which the highest tension forces are measured during the seismic excitations. Furthermore, a typical inverse proportional relationship between reliability and redundancy, where higher reliability corresponds to lower redundancy, is observed in the numerical example.

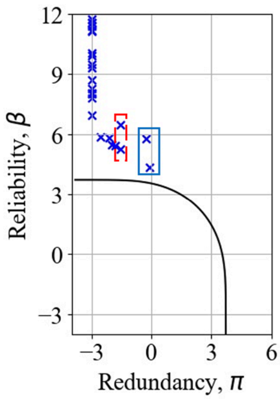

Figure 20. β−π diagram of the cable-stayed bridge

5. Conclusions

This study newly established a resilience assessment framework for structures subjected to external forces having high aleatory uncertainties from a system-reliability-based perspective. The framework leveraged the concept of reliability and redundancy curves to accommodate the aleatoric variabilities in excitation. Using these curves, a pair of reliability and redundancy indices were estimated for each mutually exclusive and collectively exhaustive (MECE) initial disruption scenario, which was then evaluated by the factored *de minimis* level of risk that considers the recoverability of each failure scenario and the number of MECE events. To facilitate a comprehensive understanding of the proposed concept, we presented and summarized five core elements needed to successfully assess the resilience performance of structures subjected to stochastic excitations. Furthermore, to increase the applicability of the proposed framework, efficient and effective computational procedures for calculating the reliability and redundancy curves were provided.

After describing the developed procedure using a three-story building structure, two more sophisticated structural systems were studied with an example of earthquake excitations to demonstrate the ideas and potential benefits of the proposed framework. The numerical investigation confirmed that the proposed framework can systemically assess the disaster resilience performance of structures subjected to stochastic excitations by efficiently dealing with MECE initial failure disruption scenarios. Although the numerical investigations focused on evaluating the seismic performance, the concept can be applied to other types of hazards such as winds, waves, or vibrations from vehicles. Currently, two further studies are underway to extend the framework and enhance the applicability of the assessment procedure. First, a mathematical expression is being developed to define and quantify the recoverability index in Eq. (14). Second, the framework is being extended to consider aging infrastructure under varying environmental conditions associated with climate change. Furthermore, it is desirable to investigate the results of resilience analysis for different scales/granularities of initial disruption scenarios. A sequential decomposition approach can be employed to systematically explore the resilience of the system and provide insights into the hierarchical nature of different components to the overall system resilience. Another interesting research topic would be to further extend the proposed methods to accommodate uncertain structural properties.

The proposed resilience assessment methodology and computational procedure are expected to enhance the applicability of the framework to more complex civil engineering systems and realistic hazards, further bridging the gap between advanced reliability theories and current performance-based engineering practices.

Acknowledgment: This research was supported by the National Research Foundation of Korea (NRF) grant funded by the Korea government (MSIT) (RS-2023-00242859).

References

1. Ahern, J. (2011). From fail-safe to safe-to-fail: Sustainability and resilience in the new urban world. Landscape and Urban Planning, 100(4), 341–343.
2. Andriotis, C. P., & Papakonstantinou, K. G. (2018). Extended and generalized fragility functions. Journal of Engineering Mechanics, 144(9), 4018087.
3. ASCE. (2019). Prestandard for Performance-Based Wind Design.
4. American Society of Mechanical Engineers (ASME). 2009. Innovative Technological Institute (ITI). Washington, D.C. ASME ITI, LLC.
5. ATC-58. (2012a). Seismic performance assessment of buildings: Volume 1 (Methodology). Federal Emergency Management Agency.
6. ATC-58. (2012b). Seismic performance assessment of buildings: Volume 2 (Implementation). Federal Emergency Management Agency.
7. Boore, D. M., & Atkinson, G. M. (2008). Ground-motion prediction equations for the average horizontal component of PGA, PGV, and 5%-damped PSA at spectral periods between 0.01 s and 10.0 s. Earthquake Spectra, 24(1), 99–138.
8. Bruneau, M., Chang, S. E., Eguchi, R. T., Lee, G. C., O'Rourke, T. D., Reinhorn, A. M., Shinozuka, M., Tierney, K., Wallace, W. A., & von Winterfeldt, D. (2003). A framework to quantitatively assess and enhance the seismic resilience of communities. Earthquake Spectra, 19(4), 733–752.
9. Cimellaro, G. P., Reinhorn, A. M., & Bruneau, M. (2010). Framework for analytical quantification of disaster resilience. Engineering Structures, 32(11), 3639–3649.
10. Cornell, C. A. (1976). Engineering seismic risk analysis, Bulletin of the Seismological Society of America.
11. Cornell, C. A., Jalayer, F., Hamburger, R. O., & Foutch, D. A. (2002). Probabilistic basis for 2000 SAC federal emergency management agency steel moment frame guidelines. Journal of Structural Engineering, 128(4), 526–533.
12. der Kiureghian, A. (2005). First-and second-order reliability methods. Engineering Design Reliability Handbook, 14.
13. Didier, M., Broccardo, M., Esposito, S., & Stojadinovic, B. (2018). A compositional demand/supply framework to quantify the resilience of civil infrastructure systems (Re-CoDeS). Sustainable and Resilient Infrastructure, 3(2), 86–102.
14. Ellingwood, B. R. (2006). Mitigating risk from abnormal loads and progressive collapse. Journal of Performance of Constructed Facilities, 20(4), 315–323.
15. Ernst, J. H. (1965). Der E-Modul von Seilen unter berucksichtigung des Durchhanges. Der Bauingenieur, 40(2), 52–55.
16. Hohenbichler, M., & Rackwitz, R. (1982). First-order concepts in system reliability. Structural safety, 1(3), 177-188.
17. Hosseini, S., Barker, K., & Ramirez-Marquez, J. E. (2016). A review of definitions and measures of system resilience. Reliability Engineering & System Safety, 145, 47–61.
18. Jiang, J., Zhang, Q., Li, L., Chen, W., Ye, J., & Li, G.-Q. (2020). Review on quantitative measures of robustness for building structures against disproportionate collapse. International Journal of High-Rise Buildings, 9(2), 127–154.

19. Kim, T., Kwon, O.-S., & Song, J. (2021a). Clustering-based adaptive ground motion selection algorithm for efficient estimation of structural fragilities. Earthquake Engineering & Structural Dynamics, 50(6), 1755–1776.
20. Kim, T., Kwon, O.-S., & Song, J. (2021b). Seismic performance of a Long-Span Cable-stayed bridge under spatially varying bidirectional spectrum-compatible ground motions. Journal of Structural Engineering, 147(4), 4021015.
21. Kramer, S. L. (1996). Geotechnical earthquake engineering, Prentice-Hall, New Jersey.
22. Li, Q. (2006). Mathematical formulation of tools for assessment of fragility and vulnerability of damaged buildings. Georgia Institute of Technology.
23. Liang, H., & Xie, Q. (2021). System vulnerability analysis simulation model for substation subjected to earthquakes. IEEE Transactions on Power Delivery.
24. Lim, S., Kim, T., & Song, J. (2022). System-reliability-based disaster resilience analysis: Framework and applications to structural systems. Structural Safety, 96. https://doi.org/10.1016/j.strusafe.2022.102202
25. Long, J. S., & Freese, J. (2006). Regression models for categorical dependent variables using Stata (Vol. 7). Stata press.
26. McKenna, F. (2011). OpenSees: a framework for earthquake engineering simulation. Computing in Science & Engineering, 13(4), 58–66.
27. Nielson, B. G., & DesRoches, R. (2007). Analytical seismic fragility curves for typical bridges in the central and southeastern United States. Earthquake Spectra, 23(3), 615–633.
28. Ohtori, Y., Christenson, R. E., Spencer Jr, B. F., & Dyke, S. J. (2004). Benchmark control problems for seismically excited nonlinear buildings. Journal of Engineering Mechanics, 130(4), 366–385.
29. Padgett, J. E., & DesRoches, R. (2008). Methodology for the development of analytical fragility curves for retrofitted bridges. Earthquake Engineering & Structural Dynamics, 37(8), 1157–1174.
30. Pang, Y., Wu, X., Shen, G., & Yuan, W. (2014). Seismic Fragility Analysis of Cable-Stayed Bridges Considering Different Sources of Uncertainties. Journal of Bridge Engineering, 19(4), 04013015. https://doi.org/10.1061/(ASCE)BE.1943-5592.0000565
31. Paté-Cornell, M. E. (1994). Quantitative safety goals for risk management of industrial facilities. Structural Safety, 13(3), 145–157.
32. Power, M., Chiou, B., Abrahamson, N., Bozorgnia, Y., Shantz, T., & Roblee, C. (2008). An overview of the NGA project. Earthquake Spectra, 24(1), 3–21.
33. Rathnayaka, B., Siriwardana, C., Robert, D., Amaratunga, D., & Setunge, S. (2022). Improving the resilience of critical infrastructure: Evidence-based insights from a systematic literature review. International Journal of Disaster Risk Reduction, 103123.
34. Shinozuka, M., Feng, M. Q., Kim, H.-K., & Kim, S.-H. (2000). Nonlinear static procedure for fragility curve development.
35. Shinozuka, M., Feng, M.Q., Kim, H., Uzawa, T., & Ueda, T. (2003). Statistical analysis of fragility curves. Technical Report MCEER.
36. Song, J., Kang, W.-H., Lee, Y.-J., & Chun, J. (2021). Structural system reliability: Overview of theories and applications to optimization. ASCE-ASME Journal of Risk and Uncertainty in Engineering Systems, Part A: Civil Engineering.
37. Tang, G. W., Li, J. Z., Tao, X. X., & others. (2008). Guidelines for seismic design of highway bridges. Ministry of Transport of the People's Republic of China, Beijing.
38. Vamvatsikos, D., & Cornell, C. A. (2002). Incremental dynamic analysis. Earthquake Engineering & Structural Dynamics, 31(3), 491–514.
39. Yi, J.-H., Kim, S.-H., & Kushiyama, S. (2007). PDF interpolation technique for seismic fragility analysis of bridges. Engineering Structures, 29(7), 1312–1322.
40. Yi, S., Papakonstantinoub, K.G., Andriotis, C.P., & Song, J. (2022). Appraisal and mathematical properties of fragility analysis methods, The 13th International Conference on Structural Safety and Reliability (ICOSSAR 2021-2022), September 13-17, Shanghai, China.
41. Zhong, J., Jeon, J.-S., Yuan, W., & DesRoches, R. (2017). Impact of spatial variability parameters on seismic fragilities of a cable-stayed bridge subjected to differential support motions. Journal of Bridge Engineering, 22(6), 4017013.